Anisotropic forward modelling of fluid injection and phase angles exceeding 90° in magnetotellurics

Thesis submitted in accordance with the requirements of the University of Adelaide for an Honours Degree in Geophysics.

Jake Macfarlane

October 2012

THE UNIVERSITY *of* ADELAIDE

ABSTRACT

Electrical anisotropy, defined as the directional dependence of electrical conductivity within a medium, causes changes in the electromagnetic signal measured by magnetotellurics (MT) and as such is an important property to consider when interpreting MT data. This study concentrates on replicating the MT response measured at two distinctively different geological settings using a series of 2-dimensional anisotropic forward models. Results presented in this study show that 2-dimensional anisotropic forward modelling is able to account for subtle differences in subsurface anisotropic resistivity structures. Specifically, 2-dimensional anisotropic forward modelling is able to reproduce the measured difference in MT response between pre- and post fluid injection conditions at the Paralana Geothermal System using an anisotropic fluid volume. A second application in constraining the source of the anomalous phase angles exceeding 90° observed in MT measurements of the Capricorn Orogen, shows that 2-dimensional anisotropic MT models are not able to produce phase angles exceeding 90° in the MT data which has its electric field orientated perpendicular to the geoelectric strike. These findings provide a case supporting the use of 2-dimensional anisotropic forward modelling as a means of modelling changes caused by the flow of a fluid through the crust. In addition, they also highlight issues associated with its application to complicated structures perpendicular to the strike of the profile.

KEYWORDS

Table of Contents

List of Figures

INTRODUCTION

Despite electrical anisotropy being an important electrical property of the Earth's interior, its identification and influence on magnetotelluric (MT) measurements is still under investigation (Kurtz et al. 1993; Ji et al. 1996; Heise & Pous 2003; Eaton et al. 2004; Simpson & Tommasi 2005; Hamilton et al. 2006; Heise et al. 2006; Chen 2009).

Recent studies of the Paralana Geothermal System in South Australia have interpreted preferentially orientated micro-fractures trending towards the north-east from changes in both the micro-seismic (Hasting et al. 2011) and the MT (Peacock et al. 2012) responses measured during fracture stimulation experiments. When combined with previous work on anisotropy, these micro-fractures may be used as an indicator for the presence of electrical anisotropy within this region (Anderson et al. 1974; Kurtz et al. 1993; Simpson & Tommasi 2005).

This information leads to the question of whether MT measurements are sensitive to subtle variations in subsurface anisotropic resistivity structures, from which we then consider whether electrical anisotropy is able to reproduce the change in MT response measured between pre- and post-fluid injection conditions measured at the Paralana Geothermal System by Peacock et al. (2012).

In addition, recent studies of the Capricorn Orogen in Western Australia have measured a phase shift between electromagnetic (EM) fields exceeding 90° and the alignment of long period induction arrows towards regions of enhanced conductivity within the Capricorn Orogen (Selway et al. 2009; Heinson et al. 2011) however, the causal structure is yet to be determined. As previous studies have successfully modelled similar MT responses using 2-dimensional anisotropic resistivity structures (Pek & Verner 1997; Heise & Pous 2003; Weckmann et al. 2003b; Brasse et al. 2009; Chen 2009), it is suggested that electrical anisotropy may be present within the Capricorn Orogen.

This subsequently raises the question of whether 2-dimensional anisotropic resistiv-

ity structures are able to reproduce the phase shift exceeding 90° within the Capricorn Orogen which will constrain the geological structure responsible for the measured MT response.

This study aims to answer these questions using synthetic MT data calculated using the 2-dimensional anisotropic resistivity code of Pek & Verner (1997) which allows for an arbitrarily oriented anisotropic resistivities. Residual phase tensor ellipse plots are used to show that MT is sensitive to variations between anisotropic resistivity structures as well as the changes between pre- and post-fluid injection conditions from the Paralana Geothermal System. In addition to this, phase angle plots are used to show that 2-dimensional anisotropic forward models of the Capricorn Orogen are unable to replicate the measured phase angles exceeding 90° which, instead, may be the result of galvanic distortion, a 3-dimensional resistivity structure or a combination of these proposed sources.

ELECTRICAL ANISOTROPY IN MAGNETOTELLURICS

MT is a passive EM technique for which electric $\mathbf{E}$ and magnetic $\mathbf{H}$ fields are measured in orthogonal directions at the Earth's surface which may be decoupled into a component incorporating $\mathbf{E}$-fields parallel to geoelectric strike (E-polarisation or transverse electric (TE)-mode) and a component incorporating $\mathbf{H}$-fields parallel to geoelectric strike (H-polarisation or transverse magnetic (TM)-mode) (Simpson & Bahr 2005). Central to MT is the diffusive propogation of EM waves through the Earth. This principal allows the frequency of measured EM waves to be related to a distance scale by the skin depth equation

$$\delta = \sqrt{\frac{2}{\mu_0 \sigma \omega}} \tag{1}$$

where δ is the penetration depth of the EM waves in kilometres, μ_0 is the magnetic permeability of free space ($\mu_0 = 4\pi \times 10^{-7}$ NA^{-2}), σ is a scalar conductivity value in S/m and ω is equal to $2\pi f$, where f is the frequency of the EM fields oscillations in Hz. As resistivity ρ, in Ωm, and conductivity σ are reciprocals of each other ($\sigma = 1/\rho$) and as such are used interchangeably throughout this thesis.

Two concepts which require some explanation to understand this thesis is the concept of isotropy which is the trait of having non-directional dependant properties (Thomsen 1986) and the concept of anisotropy which is the trait of having directional dependant properties (Thomsen 1986; Winterstein 1990). Electrical anisotropy is then defined as the directionally dependant relationship between current density $\mathbf{J}$ and an applied electric field $\mathbf{E}$ in the presence of an anisotropic resistivity structure (Heinson & White 2005; Wannamaker 2005).

For a simple, isotropic case with a scalar conductivity value, this relationship is governed by Ohm's law

$$\mathbf{J}(\omega) = \sigma(\omega)\mathbf{E}(\omega). \tag{2}$$

To incorporate electrical anisotropy into equation (2) we replace the scalar conductivity value σ with a 3-dimensional conductivity tensor $\hat{\sigma}$ as defined in Pek & Verner (1997)

$$\hat{\sigma} = \begin{pmatrix} \sigma_{xx} & \sigma_{xy} & \sigma_{xz} \\ \sigma_{yx} & \sigma_{yy} & \sigma_{yz} \\ \sigma_{zx} & \sigma_{zy} & \sigma_{zz} \end{pmatrix} \tag{3}$$

where x, y and z are defined as mutually orthogonal directions, with positive z downward. The conductivity tensor may also be defined as

$$\hat{\sigma} = \sigma_{ij}\hat{\mathbf{e}}_i\hat{\mathbf{e}}_j \tag{4}$$

where, for i and j $\in \{x, y, z\}$, σ_{ij} describes the linear relationship between an induced current density in the i direction due to an applied field in the j direction and the outer product $\hat{\mathbf{e}}_i \hat{\mathbf{e}}_j$ contains information regarding the coordinate system for any specific component of $\hat{\sigma}$ (Kusse & Westwig 2006). This tensor can then be diagonalised and expressed by three rotation angles α_S, α_D and α_{SL}, measured in degrees, which relate the orientation of the tensor's principal axes $\{x''', y''', z'''\}$ to the reference frame $\{x, y, z\}$ and three principal conductivities σ_x, σ_y and σ_z, measured in S/m, which define the conductivity along the x'''-, y'''- and z'''-axes respectively where $\sigma_x = \sigma_{xx}{}'''$, $\sigma_y = \sigma_{yy}{}'''$ and $\sigma_z = \sigma_{zz}{}'''$ (Figure 1)

$$\hat{\sigma} = R_z(-\alpha_S)R_{x'}(-\alpha_D)R_{z''}(-\alpha_{SL}) \underbrace{\begin{pmatrix} \sigma_x & 0 & 0 \\ 0 & \sigma_y & 0 \\ 0 & 0 & \sigma_z \end{pmatrix}}_{\sigma(x''', y''', z''')} R_z(\alpha_S)R_{x'}(\alpha_D)R_{z''}(\alpha_{SL}). \quad (5)$$

Following the notation defined in Pek & Santos (2006), R_z, $R_{x'}$ and $R_{z''}$ are rotation matrices around the coordinate axes specified by the sub-script and α_S, α_D and α_{SL} are the 'strike', 'dip' and 'slant' angles of anisotropy which are analogous to Euler's elementary rotations from classical mechanics. The successive rotations are graphically represented in Figure 1.

Using the anisotropic conductivity tensor, we then re-define Ohm's law as

$$\mathbf{J}(\omega) = \hat{\sigma}(\omega) \cdot \mathbf{E}(\omega) \quad (6)$$
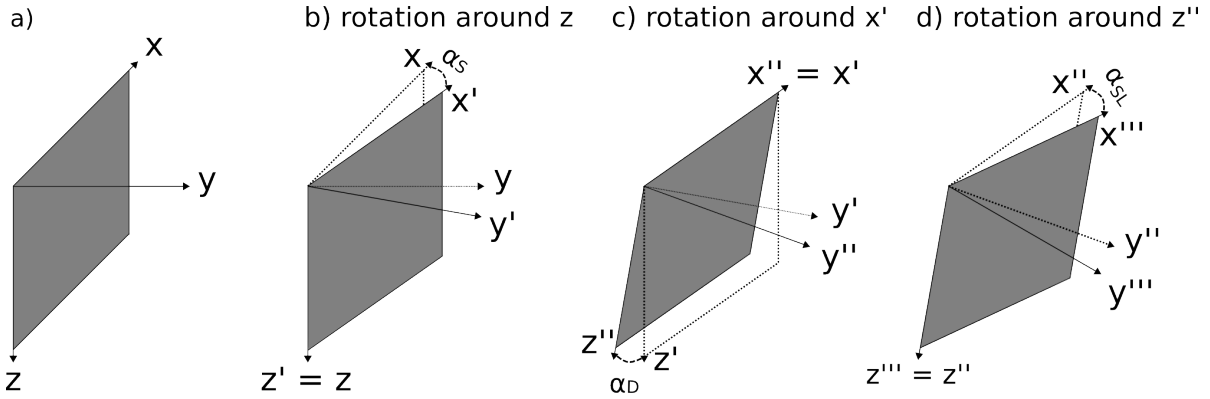
Figure 1: Successive rotations which define the conductivity tensor. The rotations are applied to the Cartesian coordinate system, {x,y,z}, where the rotation angles α_S , α_D and α_{SL}, which are the 'strike', 'dip' and 'slant' anisotropy angles, define a rotation around the z-, x' and z"-axes respectively in degrees to form the coordinate system {x''',y''',z'''} which defines the conductivity tensor's principal axes.

to correctly implement the conductivity tensor (Weiss & Newman 2002). From this, the total electric field **E** is defined in terms of an isotropic component $\mathbf{E_0}$ and an anisotropic component ($\mathbf{E'}$) (Weiss & Newman 2002)

$$\mathbf{E}(\omega) = \mathbf{E_0}(\omega) + \mathbf{E'}(\omega). \tag{7}$$

This may then be linked to an induced magnetic field **H** through the quasi-stationary approximation of Maxwell's equation (Rikitake 1948)

$$\nabla \times \mathbf{H} = \hat{\sigma}\cdot\mathbf{E}. \tag{8}$$

From the relationships defined in equations (7) and (8), it is possible to define the vertical magnetic transfer function expressed by the 'induction vector' **K**

$$H_z = -\mathbf{K}\cdot\mathbf{H} \tag{9}$$

where H_z is the vertical magnetic field, $\mathbf{H}$ is the horizontal magnetic field and the orientation of its real component is toward regions of enhanced conductivity (Caldwell et al. 2004). Similarly, the electric field transfer function may be represented by the 2-by-2 matrix, referred to as the 'impedance tensor' $\mathbf{Z}$, with each component defined by the relationship

$$Z_{ij} = \left(\frac{E_i}{H_j} \right) \tag{10}$$

where E_i defines an electric field in the i direction and H_j defines a magnetic field in the j direction (Heise & Pous 2003; Heinson & White 2005; Heise et al. 2006). In a 2-dimensional environment where the measuring orientations of an MT response are aligned parallel and perpendicular to geoelectric strike, the impedance tensor may be reduced to the anti-diagonalised form

$$\mathbf{Z}_{ij} = \begin{pmatrix} 0 & Z_{\parallel} \\ -Z_{\perp} & 0 \end{pmatrix}. \tag{11}$$

where $Z_{\parallel}$ and $Z_{\perp}$ are the TE- and TM-mode impedances respectively. In addition, this complex valued tensor may be separated into its real $\mathbf{X}$ and imaginary components $\mathbf{Y}$ to produce

$$\mathbf{Z} = \mathbf{X} + i\mathbf{Y}. \tag{12}$$

Equation 12 is then used to define the phase angle ϕ which expresses the phase shift between the electromagnetic fields measured at the surface (Heise & Pous 2003; Caldwell et al. 2004; Heise et al. 2006)

$$\phi_{ij} = \tan^{-1} \left(\frac{\Re(\mathbf{Z}_{ij})}{\Im(\mathbf{Z}_{ij})} \right). \tag{13}$$

For a homogeneous Earth, ϕ is determined by one scalar value and as such produces phase angles of 45° whereas in a 2-dimensional Earth, common values range between 0°

and 90° (Naidu 2012). However, in the event of strong current channelling, it is possible to have phase angles exceeding 90° (Egbert 1990).

For a more detailed interpretation of phase relationships, we define the phase tensor $\mathbf{\Phi}$ which expresses how the phase shift between the electromagnetic fields changes with polarisation (Caldwell et al. 2004)

$$\mathbf{\Phi} = \mathbf{X}^{-1}\mathbf{Y}. \tag{14}$$

From that we derive another matrix, the "residual phase tensor", which represents the change between post-fluid injection or anisotropic phase tensor $\hat{\mathbf{\Phi}}$ and the pre-fluid injection or isotropic phase tensor $\mathbf{\Phi}$ (Heise et al. 2007)

$$\mathbf{\Delta} = \mathbf{I}_2 - \frac{1}{2}\left(\hat{\mathbf{\Phi}}^{-1}\mathbf{\Phi} + \mathbf{\Phi}\hat{\mathbf{\Phi}}^{-1}\right)$$

where $\mathbf{I}_2$ is the 2×2 identity matrix.

APPLICATION TO FIELD DATA

In this study, MT data from two field areas were examined in an attempt to reproduce the measured MT responses at two distinctively different geological settings using 2-dimensional anisotropic resistivity structures.

Paralana Geothermal System

The Paralana Geothermal System is situated in a dilational zone along a splay off the eastward thrusting Paralana fault system (Paul et al. 1999; McLaren et al. 2002; Brugger et al. 2005) bounding the eastern margin of the Mt. Painter Domain (MPD) (Brugger et al. 2005) in the Northern Flinders Ranges, South Australia (Figure 2). The MPD con-

sists of granites, gneisses and metasediments dated at approximately 1600 Ma to 1580 Ma in age (Fanning et al. 2003; Kromkhun 2010). These units were overlain by sediments (Paul et al. 1999; McLaren et al. 2002; Brugger et al. 2005; Wülser 2009) with a maximum age of 800 Ma (Wülser 2009) and a lower age limit constrained to the initiation of the Delamerian Orogen (Wülser 2009), which occurred between 514 Ma and 492 Ma (Foden et al. 1999; Foden et al. 2006). Further granitic intrusions and tectonothermal events have been recorded throughout the history of the MPD (Wülser 2009) with the British Empire Granite intruding at approximately 460 to 440 Ma (Elburg et al. 2003; McLaren et al. 2006; Wülser 2009).

Recent MT studies of this region have assumed an isotropic resistivity structure (Thiel et al. 2011, S. Thiel pers. comm. 2012). However, previous studies have interpreted preferentially orientated micro-fractures trending towards the north-east from the micro-seismic cloud presented by Hasting et al. (2011) and magnetotelluric phase tensor ellipses presented by Peacock et al. (2012) which suggest shear wave splitting (Crampin 1978; Crampin 1981; Ji et al. 1996; Rial et al. 2005; Tang et al. 2005) and electrical anisotropy (Kurtz et al. 1993; Simpson & Tommasi 2005) may be present within this region. This then raises the question of whether MT is sensitive to subtle changes in the anisotropic resistivity structure of a region and whether magnetotellurics is able to reproduce the measured difference in MT response between pre- and post-fluid injection conditions (Peacock et al. 2012) using a 2-dimensional anisotropic resistivity structure.

Capricorn Orogen

The Capricorn Orogen in Western Australia (Figure 3) defines the oblique collision between the Pilbara and Yilgarn cratons due to a long-lived subduction related arc (Myers 1990; Tyler & Thorne 1990) constrained to approximately 2000-1600 Ma (Tyler
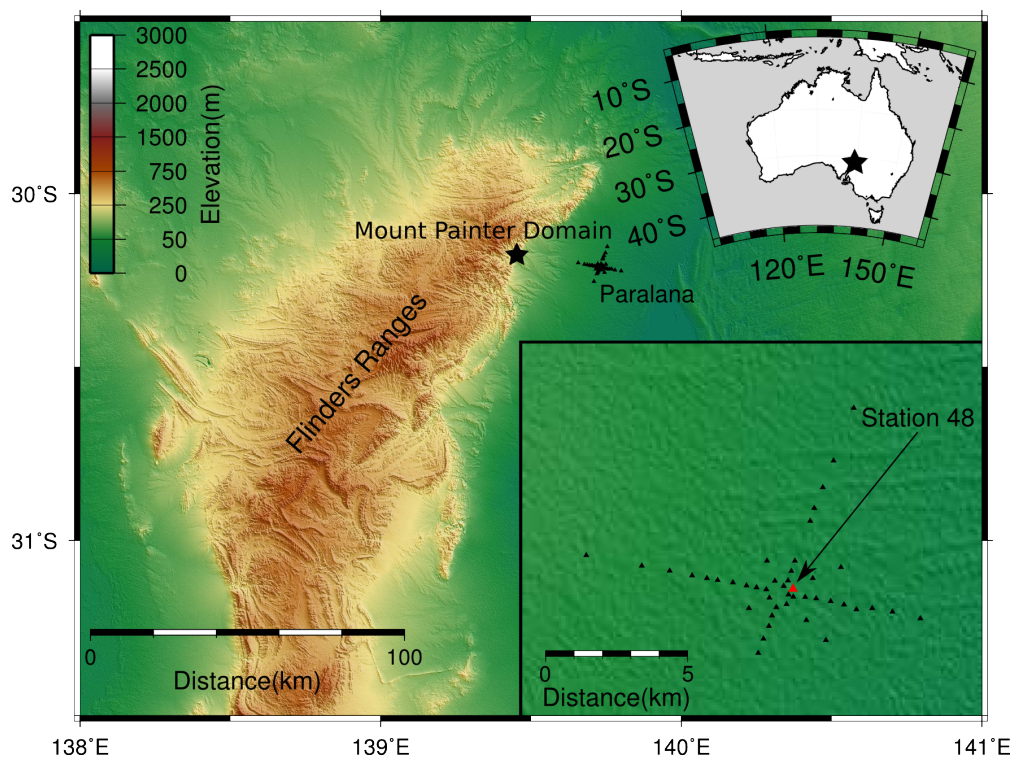
Figure 2: Location map of the Paralana Geothermal System in South Australia with MT stations (from Peacock et al. 2012) displayed as black triangles on a topography map with a star marking the Mount Painter Domain. The inset displaying a map of Australia specifies the location of the Paralana Geothermal System using a star. The inset displaying a section of the station array with increased magnification highlights station 48 (displayed in red) which was situated above the region through which fluids flowed (Peacock et al. 2012).

& Thorne 1990; Occhipinti et al. 1998; Kinny et al. 2004). The Narryer terrane defines the north-western edge of the Yilgarn Craton and consists of granites and gneisses dated to be between 3700-3300 Ma in age (Kinny et al. 1990; Nutman et al. 1991) as well as metasedimentary and metavolcanic rocks deposited and metamorphosed between 3100-2700 Ma (Kinny et al. 1990; Nutman et al. 1991). These rocks were then intruded by a series of granites and gabbro sheets at approximately 2750-2600 Ma (Cawood & Tyler 2004) with further granitic intrusions and metamorphism occurring at approximately 1950-1945 Ma (Kinny et al. 2004) and during the Capricorn Orogeny (Kinny et al. 2004) at approximately 1830-1780 Ma (Occhipinti et al. 1998; Kinny et al. 2004). The Pilbara

Craton consists of a basement of Paleo- to Neoarchean granites and greenstones dated to be 3720-2850 Ma (Kranendonk et al. 2002) in age which were unconformably overlain by the meta-sedimentary and volcano-sedimentary rocks of the Hamersley Basin dated to approximately 2700-2400 Ma in age (Pidgeon 1984; Arndt et al. 1991; Trendall et al. 2004).These rocks were then intruded by mafic to ultramafic sills and deformed during the Ophthalmian Orogeny at approximately 2200 Ma (Rasmussen et al. 2005) and the Capricorn Orogeny (Tyler & Thorne 1990) at approximately 1830-1780 Ma (Occhipinti et al. 1998; Kinny et al. 2004).

Recent MT studies of this region have measured phase angles exceeding 90° as well as the alignment of induction arrows at long periods (Selway et al. 2009; Heinson et al. 2011) however, the source of these MT responses is yet to be constrained. Previous studies have adequetly reproduced responses similar to those measured in the Capricorn Orogen using electrical anisotropy (Pek & Verner 1997; Heise & Pous 2003; Weckmann et al. 2003b; Brasse et al. 2009; Chen 2009), complex 3-dimensional resistivity structures (Pous et al. 2002; Lezaeta & Haak 2003; Weckmann et al. 2003a; Weckmann et al. 2003b; Ichihara & Mogi 2009; Thiel et al. 2009), or galvanic distortion (Chouteau & Tournerie 2000; Lilley & Weaver 2010). From these results, it is then questioned whether 2-dimensional anisotropic forward models are able to adequately reproduce the measured phase angles exceeding 90°.

METHOD

Inversion Modelling

The inversion model presented within the Two-Dimensional Modelling: Capricorn Orogen section was calculated from MT data obtained by Heinson et al. (2011) using the non-linear conjugate gradient inversion method of Rodi & Mackie (2001). MT data

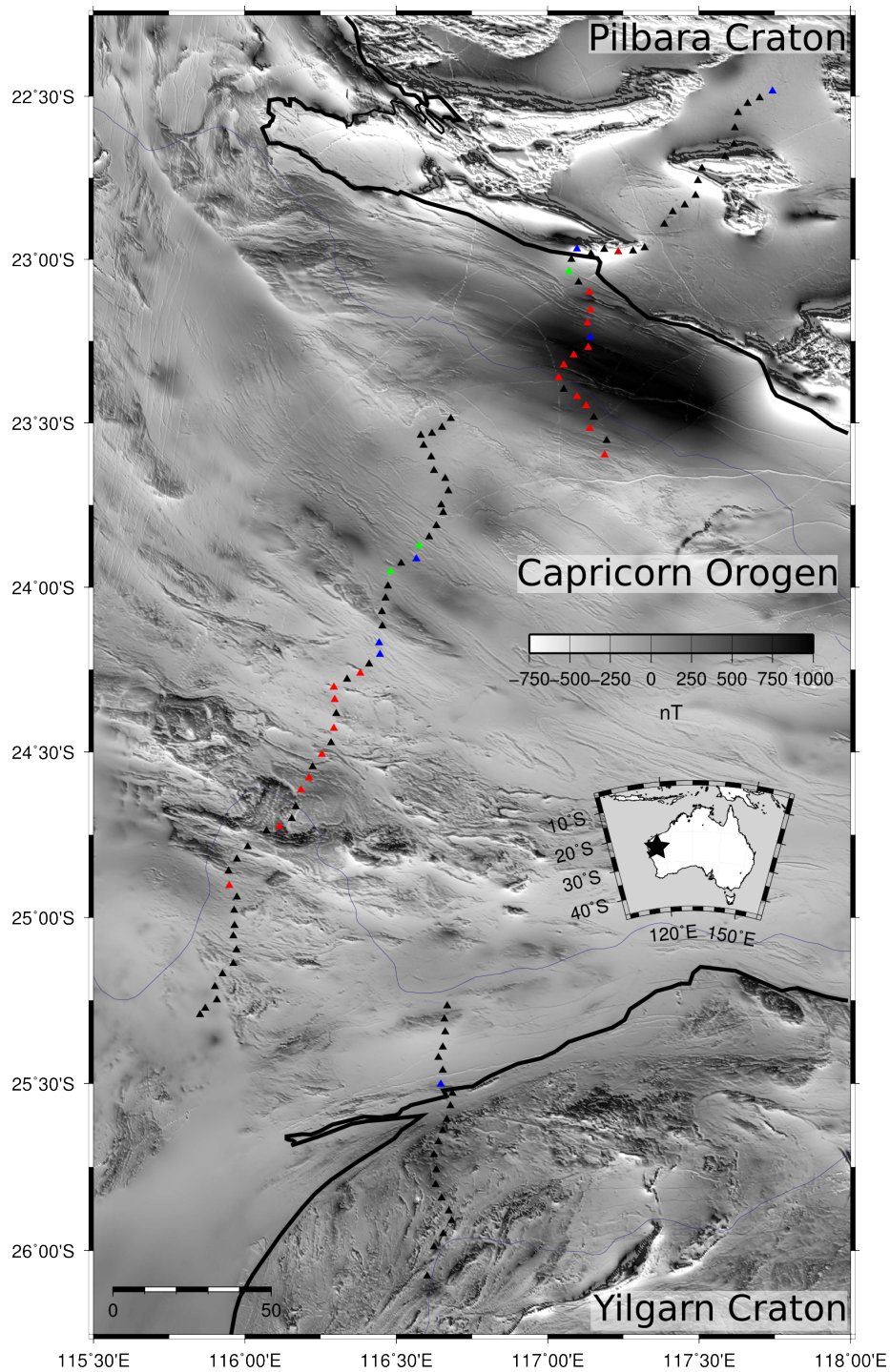**Figure 3:** Location map of the Capricorn Orogen in Western Australia with MT stations (from Heinson et al. 2011) displayed as triangles on a total magnetic intensity map. Black stations correspond to phases less than 90° in both the TE- and TM-mode, blue stations have phases greater than 90° in the TM-mode, red stations have phases greater than 90° in the TE-mode, green stations have phases greater than 90° in the TE- and TM- modes.

utilised by this inversion were collected along a line orientated 30° east from geographic north. The MT data were then rotated 60° west from geographic north such that it created an inversion model which displays the same geological structures as the forward model of the same region. In addition to this, significant masking of rotated data in both the TE-mode and TM-mode was undertaken to remove phase angles which were greater than 90° or less than 0° as they cannot be modelled using the inversion code or are considered anisotropic. Inversion modelling within this study was completed to supply additional information to constrain the geological structures input into the forward model formed for the Capricorn Orogen.

Forward Modelling

All forward models presented in this study were calculated using the 2-dimensional MT direct code for conductors with arbitrary anisotropy of Pek & Verner (1997). Modelled resistivity structures were defined in terms of their principal resistivity (ρ_x, ρ_y and ρ_z) and their anisotropy angles (α_S, α_D and α_{SL}). To reduce ambiguity and form models which approximate the true structure to the best of our knowledge, modelled resistivity structures were constrained by information interpreted from the 2-dimensional inversion models presented within the Two-Dimensional Modelling: Capricorn Orogen section and by Heinson et al. (2011) along with additional geological information (Peacock et al. 2012; Heinson et al. 2011; S. Thiel pers. comm. 2012). To further reduce ambiguity, the resistivity values assigned to each modelled structure approximated those displayed by the 2-dimensional inversion models presented within the Two-Dimensional Modelling: Capricorn Orogen section and by Heinson et al. (2011) along with known fluid resistivities (Peacock et al. 2012).

The synthetic MT responses were then plotted using Matlab codes to display phase angles in degrees and residual phase tensor ellipses. The latter displayed the differ-

ence in MT response between isotropic and anisotropic resistivity structures or pre- and post-fluid injection conditions, the orientation which experienced the greatest conductivity contrast between the two scenarios and the geometric mean of the maximum and minimum phase ($\sqrt{\triangle\phi_{max}\triangle\phi_{min}}$) providing a measure of the phase averaged over polarisation direction (Heise et al. 2008) which are represented by the the area of an ellipse, the long axis of an ellipse and the colours used to fill the ellipses respectively. A detailed description of the codes used in this study is presented in Appendix A: Detailed Method.

TWO-DIMENSIONAL MODELLING

Paralana Geothermal System

Figure 4 displays the modelled resistivity structure for the Paralana Geothermal System from which the synthetic isotropic and anisotropic MT responses were calculated. Forward models of this region consisted of three isotropic layers extending horizontally throughout the entire model and a discrete block at a depth of approximately three kilometres within the centre of the model which had a resistivity structure that was varied between isotropic and anisotropic. The background resistivity for both the isotropic and anisotropic models was defined as $500\ \Omega m$ by the horizontal isotropic layer which hosted the block.

Figures 5 and 6 present residual phase tensor ellipses showing measurable changes in MT information between isotropic and anisotropic resistivity structures with arbitrary values for α_S, α_D, ρ_x and ρ_z assigned to the anisotropic forward models. Figure 7 presents synthetic (a) and measured (b) residual phase tensor ellipses and show similar changes in MT response measured between isotropic and anisotropic resistivity structures, and pre- and post-fluid injection conditions at station 48 which was the closest station to the Paralana injection site (Figure 2).
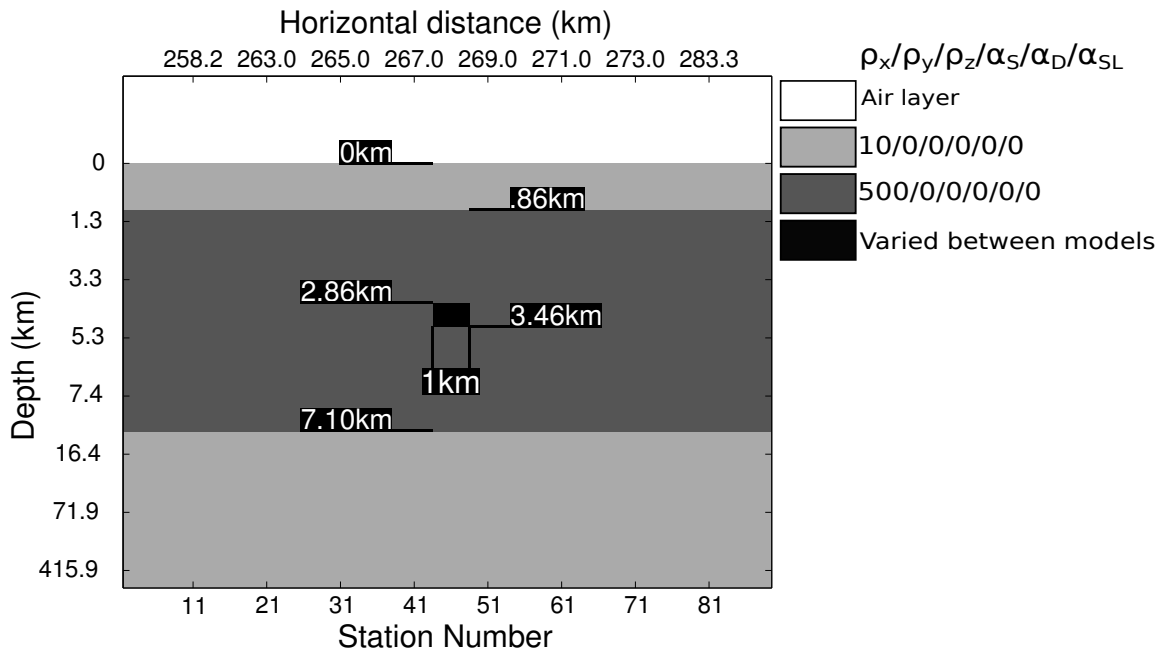
Figure 4: Model of the resistivity structure from the Paralana Geothermal System which was input into the 2-dimensional MT direct code for conductors with arbitrary anisotropy (Pek & Verner, 1997). The block situated at depth in the centre of the model was varied between an isotropic or anisotropic resistivity structure. The values displayed in the scale define the principal resistivity along the x-, y- and z-axes (ρ_x, ρ_y, ρ_z respectively) defined in Ωm and the anisotropy angles strike, dip and slant (α_S, α_D, α_{SL} respectively) defined in degrees. The values displayed within the image itself define the depth to each interface in kilometres and the width in kilometres where applicable assigned to each resistivity domain.

Figure 5: Graphical representation of the difference in MT response with respect to period (seconds) for isotropic and anisotropic configurations of the Paralana Geothermal System forward model with varying anisotropy angles α_S and α_D. The values displayed in the scale define the principal resistivity along the x-, y- and z-axes (ρ_x, ρ_y, ρ_z respectively) defined in Ωm and the anisotropy angles strike, dip and slant (α_S, α_D, α_{SL} respectively) defined in degrees. Magnetotelluric responses displayed correspond to variations in the MT response caused by changing α_S and α_D for the anisotropic block at depth whereas MT responses. The colours used to fill the ellipses themselves shows the geometric mean of the maximum and minimum phase which provides a measure of the phase averaged over polarisation direction (Heise et al. 2008).
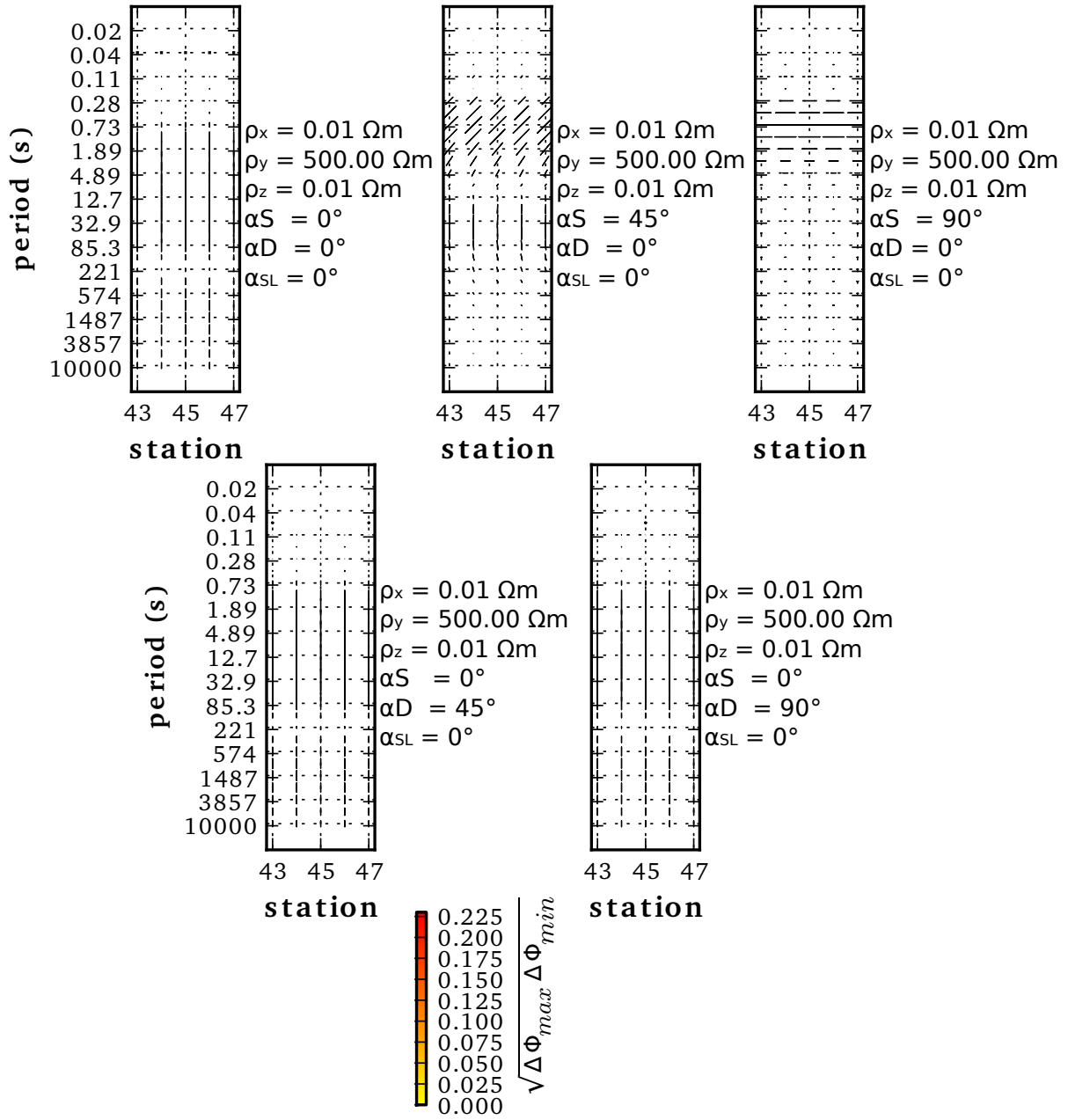
Figure 6: Graphical representation of the difference in MT response with respect to period (seconds) for isotropic and anisotropic configurations of the Paralana Geothermal System forward model with varying resistivities. The values displayed in the scale define the principal resistivity along the x-, y- and z-axes (ρ_x, ρ_y, ρ_z respectively) defined in Ωm and the anisotropy angles strike, dip and slant (α_S, α_D, α_{SL} respectively) defined in degrees. Magnetotelluric responses displayed correspond to variations in the MT response caused by changing ρ_x and ρ_z for the anisotropic block at depth. The colours used to fill the ellipses themselves shows the geometric mean of the maximum and minimum phase which provides a measure of the phase averaged over polarisation direction (Heise et al. 2008).
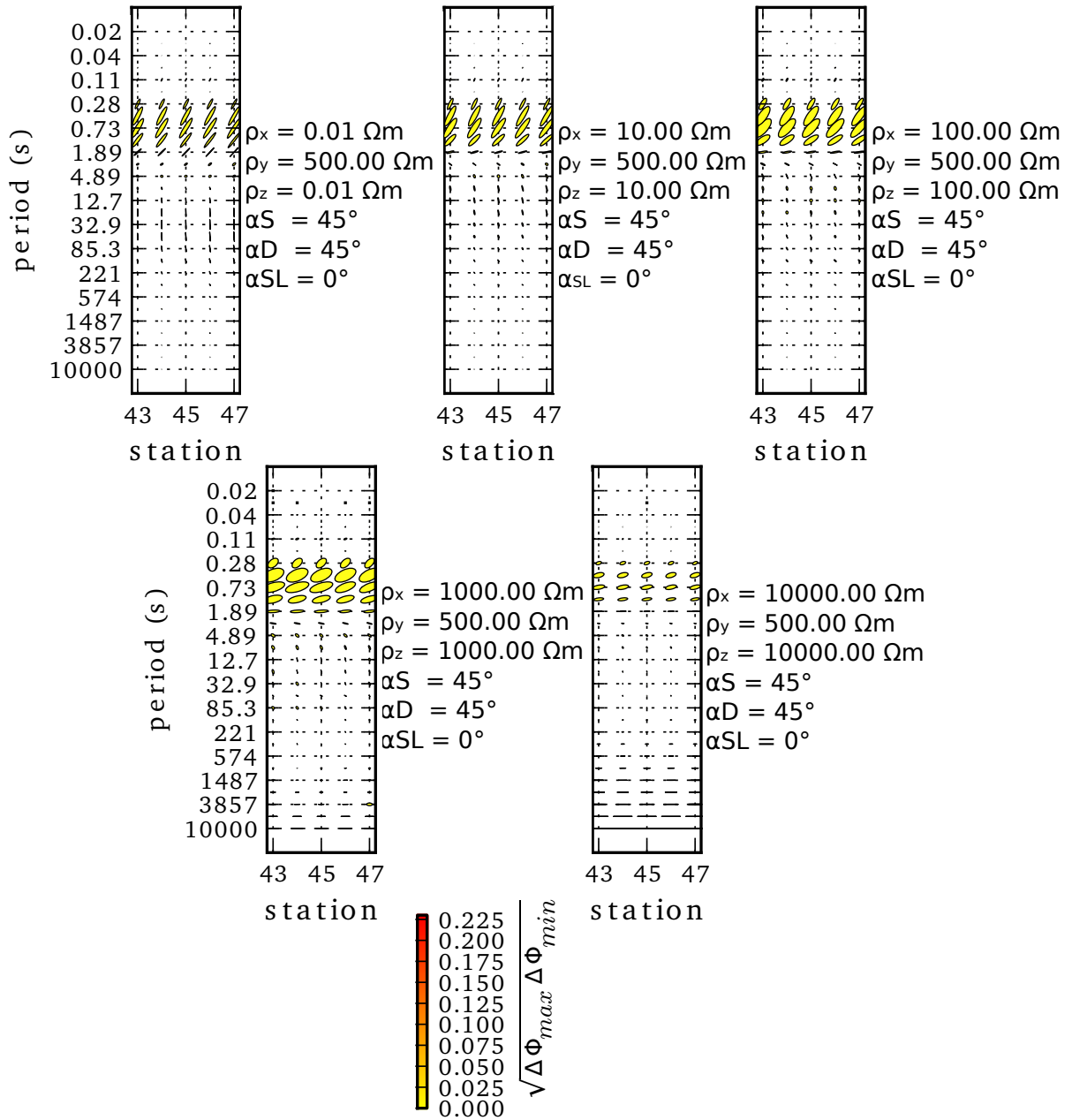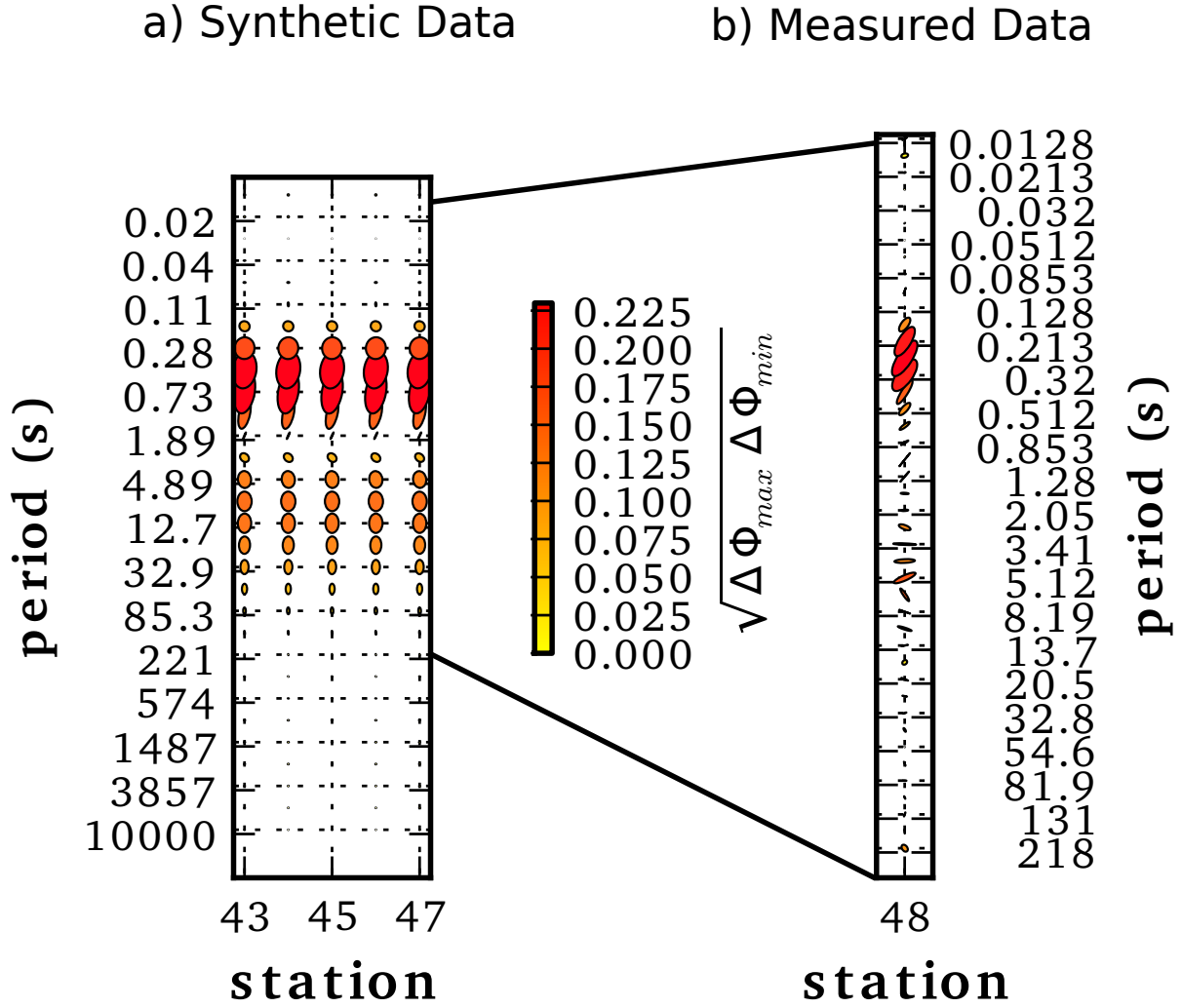
Figure 7: Graphical representation of the difference in MT response with respect to period (seconds). (a) displays the difference in MT information between an isotropic configuration, with the discrete block at depth defined with $\rho_x = \rho_y = \rho_z = 500\Omega m$ and $\alpha_S = \alpha_D = \alpha_{SL} = 0°$, and an anisotropic configuration, with the discrete block at depth defined with $\rho_x = \rho_z = 0.01\Omega m$, $\rho_y = 500\Omega m$, $\alpha_S = 10°$, $\alpha_D = 30°$ and $\alpha_{SL} = 0°$ and $\alpha_S = \alpha_D = \alpha_{SL} = 0°$, of the forward model presented in Figure 4. (b) displays the measured difference in MT information between pre- and post-fluid injection conditions measured at station 48 (Peacock et al. 2012). The values defining the forward model correspond to the principal resistivity along the x-, y- and z-axes (ρ_x, ρ_y, ρ_z respectively) defined in Ωm and the anisotropy angles strike, dip and slant (α_S, α_D, α_{SL} respectively) defined in degrees. The colours used to fill the ellipses themselves shows the geometric mean of the maximum and minimum phase which provides a measure of the phase averaged over polarisation direction (Heise et al. 2008). It is important to appreciate the different period scales defining the two plots as, following the skin depth equation ($\delta = \sqrt{\frac{2}{\mu_0 \sigma \omega}}$), corresponds to different depth scales.

Capricorn Orogen

The inversion model presented in Figure 8 was calculated for the 10GA-CP1 line from Heinson et al. (2011) with a final smoothing factor: $\tau = 3$, weighting functions: $\beta = \alpha = 1$ and error floors: $Err_{\sigma_{TE}} = 50\ \%$, $Err_{\sigma_{TM}} = 20\ \%$, $Err_{\phi_{TE}} = 10\ \%$ and $Err_{\phi_{TM}} = 8\ \%$ resulting in an rms of 1.63 which could not be reduced within additional iterations.

Significant variations between inversion models presented in this study and in Heinson et al. (2011) are likely to be due to differences in rotation angle applied to the data with the model presented in Heinson et al. (2011) rotated 30° east of geographical north. This 90° difference in rotation angle resulted in the inversion model presented in Figure 8 to be perpendicular to the model presented in Heinson et al. (2011), subsequently causing each model to show different geological structures. Additional differences are likely to be the result of variations in the amount of data with phase angles above 90° and below 0° removed from the inversion model.

Figures 9, 10 and 11 display the three modelled resistivity structures for the Capricorn Orogen from which anisotropic synthetic MT responses are calculated. Modelling of this region consisted of two isotropic resistivity domains and two anisotropic resistivity domains defined to occur within the model.

Figure 12 displays the synthetic phase angle (degrees) response calculated for three different anisotropic forward models along with the measured phase angle (degrees) response from station 32 within line 10GA-CP1 from Heinson et al. (2011).
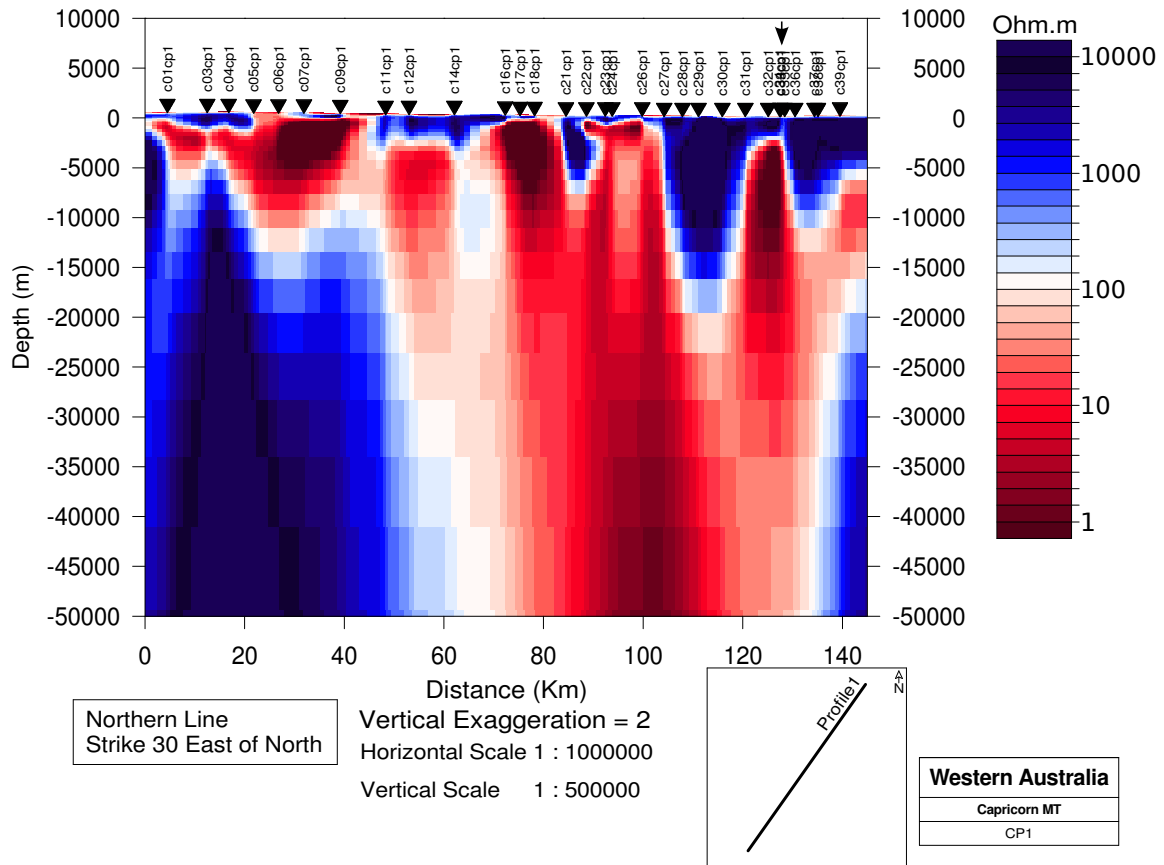
Figure 8: Inversion model of the 10GA-CP1 line from Heinson et al. (2011) using the non-linear conjugate gradients inversion algorithm of Rodi and Mackie (2001). This inversion used both TE and TM components of the data formed using a smoothing factor: $\tau = 3$, weighting functions: $\beta = \alpha = 1$ and error floors: $Err_{\sigma_{TE}} = 50$ %, $Err_{\sigma_{TM}} = 20$ %, $Err_{\phi_{TE}} = 10$ % and $Err_{\phi_{TM}} = 8$ % resulting in an rms of 1.63 which could not be reduced any further by additional iterations. Masking was undertaken to remove MT responses with phase angles greater than 90° or less than 0° as well as responses containing large amounts of noise. A resistivity domain with a high conductivity in this image is represented by the colour red where a high resistivity is represented by a blue colour. The displayed arrow marks the central point of the five kilometre wide region which was forward modelled.

Figure 9: Model of the resistivity structure from the Capricorn Orogen which was input into the 2-dimensional MT direct code for conductors with arbitrary anisotropy (Pek & Verner, 1997). The values displayed in the scale define the principal resistivity along the x-, y- and z-axes (ρ_x, ρ_y, ρ_z respectively) defined in Ωm and the anisotropy angles strike, dip and slant (α_S, α_D, α_{SL} respectively) defined in degrees. The values displayed within the image itself define the depth to each interface in kilometres and the width in kilometres where applicable assigned to each resistivity domain.
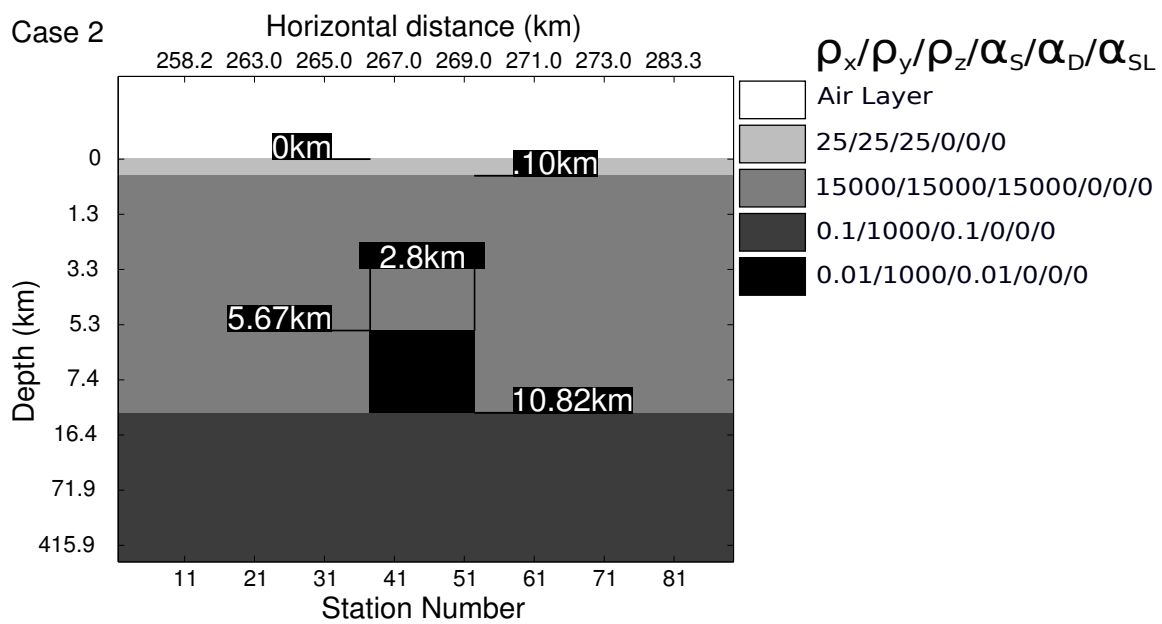
Figure 10: Model of the resistivity structure from the Capricorn Orogen which was input into the 2-dimensional MT direct code for conductors with arbitrary anisotropy (Pek & Verner, 1997). The values displayed in the scale define the principal resistivity along the x-, y- and z-axes (ρ_x, ρ_y, ρ_z respectively) defined in Ωm and the anisotropy angles strike, dip and slant (α_S, α_D, α_{SL} respectively) defined in degrees. The values displayed within the image itself define the depth to each interface in kilometres and the width in kilometres where applicable assigned to each resistivity domain.
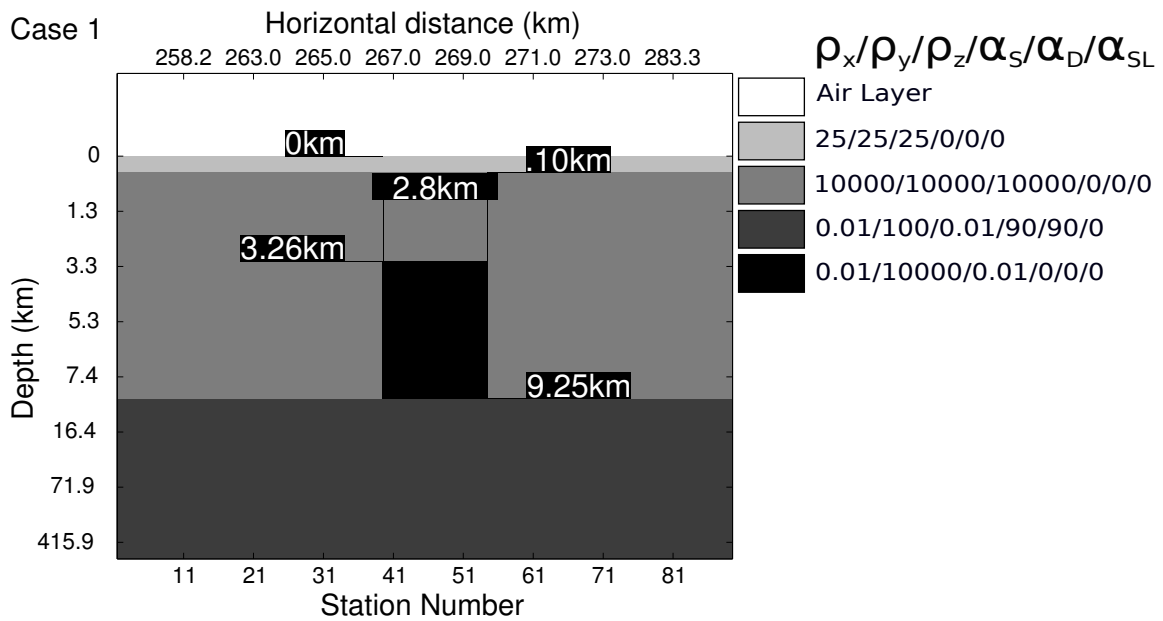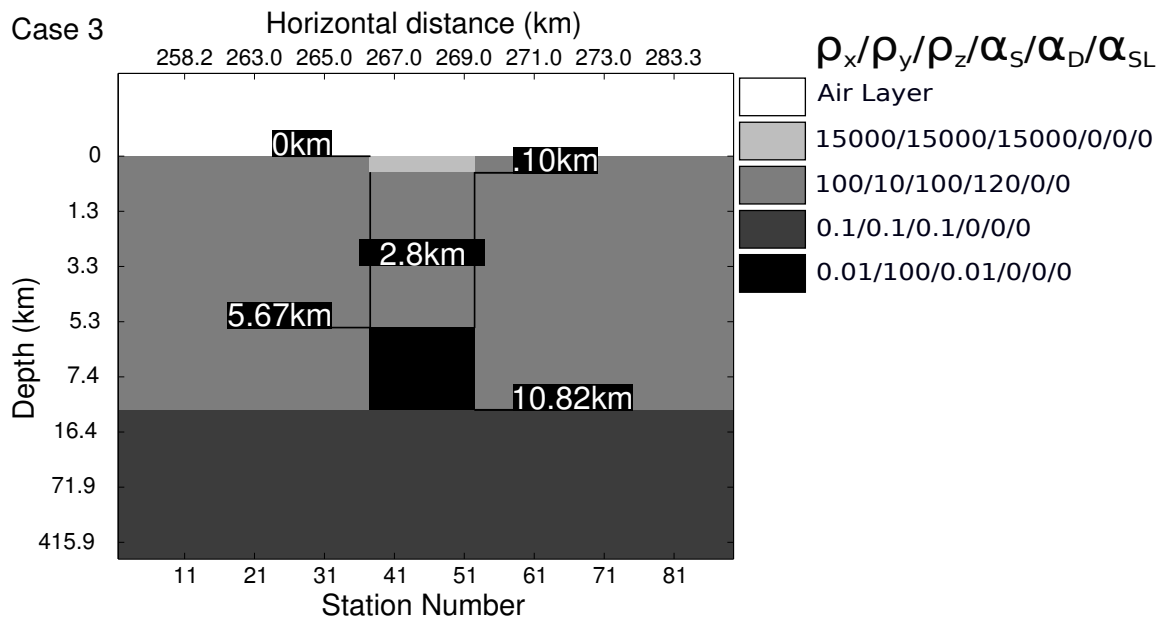
Figure 11: Model of the resistivity structure from the Capricorn Orogen which was input into the 2-dimensional MT direct code for conductors with arbitrary anisotropy (Pek & Verner, 1997). The values displayed in the scale define the principal resistivity along the x-, y- and z-axes (ρ_x, ρ_y, ρ_z respectively) defined in Ωm and the anisotropy angles strike, dip and slant (α_S, α_D, α_{SL} respectively) defined in degrees. The values displayed within the image itself define the depth to each interface in kilometres and the width in kilometres where applicable assigned to each resistivity domain.
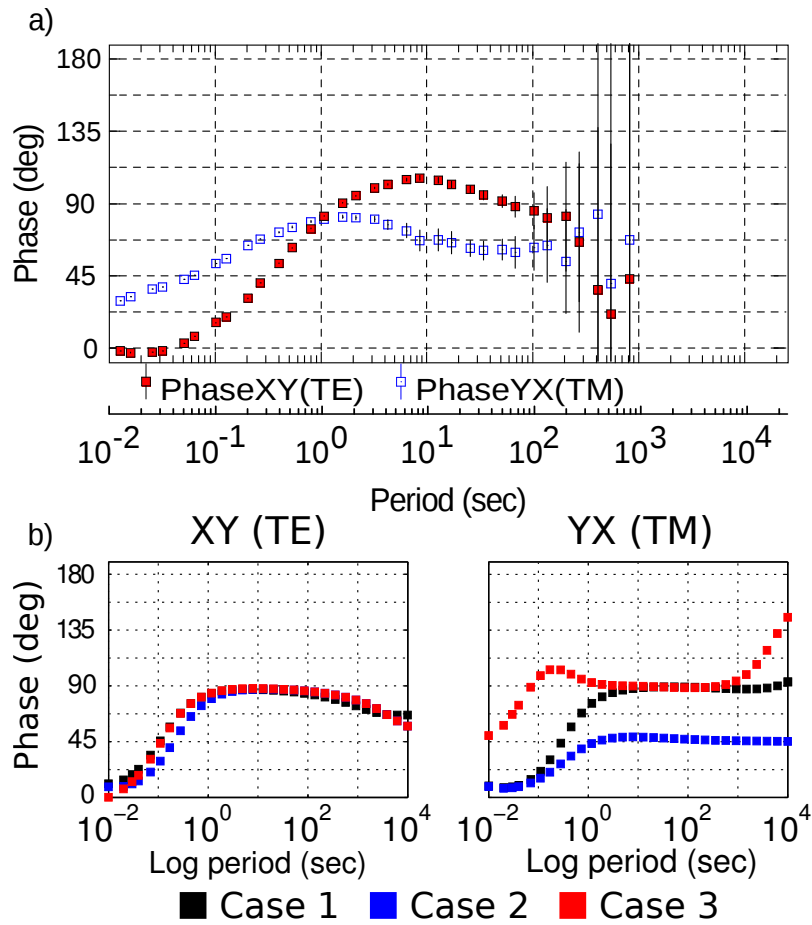
Figure 12: (a) displays the Measured MT data for station 32 within line 10GA-CP1, taken from (Heinson et al. 2011) presented to highlight the observed phase angles exceeding 90°. (b) displays synthetic phase angle response curves for the forward model of the Capricorn Orogen created by the 2-dimensional MT direct code for conductors with arbitrary anisotropy (Pek & Verner, 1997). The coloured response curves displayed in (b) correspond to the modelled resistivity structures specified in Figures 9, 10 and 11.

DISCUSSION

Geophysical Ambiguity

It is important to note that each geophysical model within this thesis suffers from ambiguity issues which are intrinsic to all geophysical modelling. Despite this, constrains

from previous geological and geophysical information allows for adequet interpretations to be made.

Influence of anisotropic model parameters on magnetotelluric responses

Residual phase tensor ellipses presented in Figure 5 show MT responses calculated for varying anisotropy angles. The orientation which experienced the greatest conductivity contrast between isotropic and anisotropic MT responses appeared to align itself parallel to the strike of the anisotropic block, with the the perpendicular orientation experiencing no measurable change. Residual phase tensor ellipses presented in Figure 6 show measurable changes in the synthetic MT response for varying resistivity values assigned to ρ_x and ρ_z. The MT response calculated for configurations with values of ρ_x and ρ_z which were significantly different to the background resistivity resulted in a decreasing difference in MT information, whereas the MT response calculated for configurations with values of ρ_x and ρ_z which were approximately equal to the background resistivity resulted in an increasing difference in MT information.

Following the measurable differences observed for all presented resistivity structures, it was interpreted that MT is sensitive to subtle changes in the anisotropic resistivity structure of a region. The dominant variables related to measurable change between varying anisotropic models were interpreted to be α_S which had an observed relationship to the orientation of the polarisation recording the largest change in MT response and the ratio of ρ_x and ρ_z with ρ_y which was observed to be related to the amount of change in MT response along with the orientation of the polarisation which measured the most significant change in MT response. In this study the anisotropic slant angle (α_{SL}) was excluded from any form of analysis as it results in a rotation around the same axis as anisotropic strike (α_S) when the anisotropic dip angle (α_D) is equal to 0°.

Therefore, a complex representation of the resistivity structures displayed in Figure 4 which experienced multiple rotations to its anisotropic structure would be required to create a measurable difference in the measured MT response.

Replicating fluid injection using anisotropy

Residual phase tensor ellipses presented in Figure 7 show similarities in the difference between pre- and post-fluid injection conditions (b) when compared to the difference between anisotropic and isotropic models (a). For periods less than 0.1 second, it is observed that both sets of ellipses display a non-responsive change. The ellipses produced for periods between 0.1 second and 1 second, interpreted to be the period range defining the preferentially orientated micro-fractures, appear to display similar MT responses with both having a polarisation of greatest change orientated at approximately 30° and an approximately equal geometric mean between the maximum and minimum phase. Differences in MT response only appear to be evident at periods greater than 1 second, with differences in both the orientation and magnitude of conductivity between MT responses observed for all later periods, which was interpreted to be due to the diffusive nature of MT which subsequently causes the modelled response to remain sensitive to the anisotropic block even at extremely long periods.

The observed similarity between synthetic and measured MT responses for the period range corresponding to the preferentially orientated micro-fractures was subsequently interpreted as evidence supporting the claim that a 2-dimensional anisotropic forward model is able to reproduce the measured change in an MT response between pre- and post-fluid injection conditions within an Enhanced Geothermal System.

These interpretations subsequently lead to the proposition that 2-dimensional anisotropic forward modelling is a feasible method of modelling the changes to an MT response due

to the flow of a fluid through the crust however, further work is required to assess its capabilities.

Phase angles exceeding 90° within the Capricorn Orogen

The plots presented in Figure 12 show that, for all period ranges, 2-dimensional anisotropic forward models were unable to produce TE-mode phase angles which exceed 90° with all cases resulting in phase angles reaching a maximum of approximately 85°. In addition to this, these images also show that the 2-dimensional anisotropic forward models defined as Case 1 and Case 3 in Figure 12 were able to produce TM-mode phase angles exceeding 90°.

The restriction of TE-mode phase angles to less than 90° was interpreted to be caused by the homogeneous extension of 2-dimensional resistivity structures perpendicular to plane of the profile subsequently removing complex interfaces which may be measured by the TE-mode. This interpretation is supported by the TM-mode phase angle response which measures numerous vertical interfaces defined within the plane of the profile and was observed to exceed 90° for two of the three presented cases.

Subsequently, it is proposed that the forward models presented in this study provide no new information to constrain the resistivity structure which produces the TE-mode phase angles exceeding 90° within the Capricorn Orogen. Additional work, in the form of 3-dimensional forward modelling, is suggested to assess whether the measured phase angles exceeding 90° are reproducible when assuming galvanic distortion, a 3-dimensional resistivity structure, or a combination of the proposed sources is present.

CONCLUSIONS

The main result presented in this study shows that 2-dimensional anisotropic forward models are able to measure subtle differences between various anisotropic resistivity

structures as well as the measured difference in MT response between pre- and post fluid injection conditions. In addition, it is shown that 2-dimensional anisotropic MT models are unable to reproduce phase angles exceeding 90° in the TE-mode interpreted to be the result of features in the x-direction being extended to infinity. These findings provide a case which supports the use of 2-dimensional anisotropic forward modelling as a method of modelling the changes caused by the flow of a conductive material through the crust however, its application to complicated structures perpendicular to the strike of the profile is limited. In addition, these findings also suggest that 3-dimensional forward modelling may be required to adequtely reproduce the measured MT response within the Capricorn Orogen.

ACKNOWLEDGMENTS

REFERENCES

Anderson, D. L., Minster, B. & Cole, D. (1974). The Effect of Oriented Cracks on Seismic Velocities, *J. Geophys. Res.* **79**(26): 4011–4015.

Arndt, N. T., Nelson, D. R., Compston, W., Trendall, A. F. & Thorne, A. M. (1991). The age of the Fortescue Group, Hamersley Basin, Western Australia, from ion microprobe zircon U-Pb results, *Australian Journal of Earth Sciences* **38**(3): 261–281.

Brasse, H., Kapinos, G., Li, Y., Mütschard, L., Soyer, W. & Eydam, D. (2009). Structural electrical anisotropy in the crust at the South-Central Chilean continental margin as inferred from geomagnetic transfer functions, *Physics of the Earth and Planetary Interiors* **173**(1–2): 7–16.

Brugger, J., Long, N., McPhail, D. & Plimer, I. (2005). An active amagmatic hydrothermal system: The Paralana hot springs, Northern Flinders Ranges, South Australia, *Chemical Geology* **222**(1–2): 35–64.

Caldwell, T. G., Bibby, H. M. & Brown, C. (2004). The magnetotelluric phase tensor, *Geophysical Journal International* **158**(2): 457–469.

Cawood, P. A. & Tyler, I. M. (2004). Assembling and reactivating the Proterozoic Capricorn Orogen: lithotectonic elements, orogenies, and significance, *Precambrian Research* **128**(3–4): 201–218.

Chen, X. (2009). From forward modelling of MT phases over 90° towards 2D anisotropic inversion, *Schmucker-Weidelt-Kolloquium fr Elektromagnetische Tiefenforschung, Heimvolkshochschule am Seddiner*.

Chouteau, M. & Tournerie, B. (2000). Analysis of magnetotelluric data showing phase rolling out of quadrant (PROQ), *SEG Technical Program Expanded Abstracts* **19**(1): 344–346.

Crampin, S. (1978). Seismic-wave propagation through a cracked solid: polarization as a possible dilatancy diagnostic, *Geophysical Journal of the Royal Astronomical Society* **53**(3): 467–496.

Crampin, S. (1981). A review of wave motion in anisotropic and cracked elastic-media, *Wave Motion* **3**(4): 343 – 391.

Eaton, D. W., Jones, A. G. & Ferguson, I. J. (2004). Lithospheric anisotropy structure inferred from collocated teleseismic and magnetotelluric observations: Great Slave Lake shear zone, northern Canada, *Geophys. Res. Lett.* **31**(19): L19614–.

Egbert, G. D. (1990). Comments On 'Concerning dispersion relations for the magnetotelluric impedance tensor' By E. Yee and K. V. Paulson, *Geophysical Journal International* **102**(1): 1–8.

Elburg, M. A., Bons, P. D., Foden, J. & Brugger, J. (2003). A newly defined Late Ordovician magmatic-thermal event in the Mt Painter Province, northern Flinders Ranges, South Australia, *Australian Journal of Earth Sciences* **50**(4): 611–631.

Fanning, C. M., Teale, G. S. & Robertson, R. S. (2003). IS THERE A WILLYAMA SUPERGROUP SEQUENCE IN THE MOUNT PAINTER INLIER?, *Broken Hill Exploration Initiative*.

Foden, J., Elburg, M. A., Dougherty-Page, J. & Burtt, A. (2006). The Timing and Duration of the Delamerian Orogeny: Correlation with the Ross Orogen and Implications for Gondwana Assembly, *The Journal of Geology* **114**(2): pp. 189–210.

Foden, J., Sandiford, M., Dougherty-Page, J. & Williams, I. (1999). Geochemistry and geochronology of the Rathjen Gneiss: implications for the early tectonic evolution of the Delamerian Orogen, *Australian Journal of Earth Sciences* **46**(3): 377–389.

Hamilton, M. P., Jones, A. G., Evans, R. L., Evans, S., Fourie, C. J. S., Garcia, X., Mountford, A. & Spratt, J. E. (2006). Electrical anisotropy of South African lithosphere compared with seismic anisotropy from shear-wave splitting analyses, *Physics of The Earth and Planetary Interiors* **158**: 226–239.

Hasting, M. A., Albaric, J., Oye, V., Reid, P., Messeiller, M. & Llanos, E. (2011). Micro-seismic monitoring during stimulation at Paralana-2 South Australia, *Abstract H21E-1159 presented at 2011 Fall Meeting, AGU, San Francisco* .

Heinson, G., Boren, G., Ross, J., Campanya, J., Thiel, S. & Selway, K. (2011). The Capricorn Orogen magnetotelluric (MT) transect, *Capricorn Orogen seismic and magnetotelluric (MT) workshop 2011: extended abstracts.*

Heinson, G. & White, A. (2005). Electrical resistivity of the Northern Australian lithosphere: Crustal anisotropy or mantle heterogeneity?, *Earth and Planetary Science Letters* **232**: 157–170.

Heise, W., Bibby, H. M., Caldwell, T. G., Bannister, S. C., Ogawa, Y., Takakura, S. & Uchida, T. (2007). Melt distribution beneath a young continental rift: The Taupo Volcanic Zone, New Zealand, *Geophys. Res. Lett.* **34**(14): L14313–.

Heise, W., Caldwell, T., Bibby, H. & Brown, C. (2006). Anisotropy and phase splits in magnetotellurics, *Physics of The Earth and Planetary Interiors* **158**: 107–121.

Heise, W., Caldwell, T. G., Bibby, H. M. & Bannister, S. C. (2008). Three-dimensional modelling of magnetotelluric data from the Rotokawa geothermal field, Taupo Volcanic Zone, New Zealand, *Geophysical Journal International* **173**(2): 740–750.

Heise, W. & Pous, J. (2003). Anomalous phases exceeding 90° in magnetotellurics: anisotropic model studies and a field example, *Geophysical Journal International* **155**: 308–318.

Ichihara, H. & Mogi, T. (2009). A realistic 3-D resistivity model explaining anomalous large magnetotelluric phases: the L-shaped conductor model, *Geophysical Journal International* **179**(1): 14–17.

Ji, S., Rondenay, S., Mareschal, M. & Senechal, G. (1996). Obliquity between seismic and electrical anisotropies as a potential indicator of movement sense for ductile shear zones in the upper mantle, *Geology* **24**(11): 1033–1036.

Kinny, P. D., Wijbrans, J. R., Froude, D. O., Williams, I. S. & Compston, W. (1990). Age constraints on the geological evolution of the Narryer Gneiss Complex, Western Australia, *Australian Journal of Earth Sciences* **37**(1): 51–69.

Kinny, P., Nutman, A. & Occhipinti, S. (2004). Reconnaissance dating of events recorded in the southern part of the Capricorn Orogen, *Precambrian Research* **128**(3–4): 279 – 294.

Kranendonk, M. J. V., Hickman, A. H., Smithies, R. H., Nelson, D. R. & Pike, G. (2002). Geology and Tectonic Evolution of the Archean North Pilbara Terrain, Pilbara Craton, Western Australia, *Economic Geology* **97**(4): 695–732.

Kromkhun, K. (2010). *Petrogenesis of high heat producing granite: implication for Mt Painter Province, South Australia*, PhD thesis, University of Adelaide, School of Earth and Environmental Sciences.

Kurtz, R. D., Craven, J. A., Niblett, E. R. & Stevens, R. A. (1993). The conductivity of the crust and mantle beneath the Kapuskasing Uplift: electrical anisotropy in the upper mantle, *Geophysical Journal International* **113**(2): 483–498.

Kusse, B. R. & Westwig, E. A. (2006). *Mathematical physics: applied mathematics for scientists and engineers; 2nd ed.*, Wiley, Ithaca, NY.

Lezaeta, P. & Haak, V. (2003). Beyond magnetotelluric decomposition: Induction, current channeling, and magnetotelluric phases over 90°, *J. Geophys. Res.* **108**(B6): 2305–.

Lilley, F. E. M. & Weaver, J. T. (2010). Phases greater than 90° in MT data: Analysis using dimensionality tools, *Journal of Applied Geophysics* **70**(1): 9–16.

McLaren, S., Dunlap, W. J., Sandiford, M. & McDougall, I. (2002). Thermochronology of high heat-producing crust at Mount Painter, South Australia: Implications for tectonic reactivation of continental interiors, *Tectonics* **21**(4): 1020–.

McLaren, S., Sandiford, M., Powell, R., Neumann, N. & Woodhead, J. (2006). Palaeozoic Intraplate Crustal Anatexis in the Mount Painter Province, South Australia: Timing, Thermal Budgets and the Role of Crustal Heat Production, *Journal of Petrology* **47**(12): 2281–2302.

Myers, J. S. (1990). Precambrian tectonic evolution of part of Gondwana, southwestern Australia, *Geology* **18**(6): 537–540.

Naidu, G. (2012). Magnetotellurics: Basic Theoretical Concepts, *Deep Crustal Structure of the Son-Narmada-Tapti Lineament, Central India*, Springer Theses, Springer Berlin Heidelberg, pp. 13–35.

Nutman, A. P., Kinny, P. D., Compston, W. & Williams, I. S. (1991). SHRIMP U-Pb zircon geochronology of the Narryer Gneiss Complex, Western Australia, *Precambrian Research* **52**(3–4): 275 – 300.

Occhipinti, S. A., Sheppard, S., Nelson, D. R., Myers, J. S. & Tyler, I. M. (1998). Syntectonic granite in the southern margin of the Palaeoproterozoic Capricorn Orogen, Western Australia, *Australian Journal of Earth Sciences* **45**(4): 509–512.

Paul, E., Flöttmann, T. & Sandiford, M. (1999). Structural geometry and controls on basement-involved deformation in the northern Flinders Ranges, Adelaide Fold Belt, South Australia, *Australian Journal of Earth Sciences* **46**(3): 343–354.

Peacock, J. R., Thiel, S., Reid, P. & Heinson, G. (2012). Magnetotelluric monitoring of a fluid injection: Example from an enhanced geothermal system, *Geophys. Res. Lett.* **39**(18): L18403–.

Pek, J. & Santos, F. A. (2006). Magnetotelluric inversion for anisotropic conductivities in layered media, *Physics of the Earth and Planetary Interiors* **158**(2-4): 139 – 158.

Pek, J. & Verner, T. (1997). Finite-difference modelling of magnetotelluric fields in two-dimensional anisotropic media, *Geophysical Journal International* **128**(3): 505–521.

Pidgeon, R. T. (1984). Geochronological constraints on early volcanic evolution of the Pilbara Block, Western Australia, *Australian Journal of Earth Sciences* **31**(2): 237–242.

Pous, J., Heise, W., Schnegg, P.-A., Muñoz, G., Martí, J. & Soriano, C. (2002). Magnetotelluric study of the Las Cañadas caldera (Tenerife, Canary Islands): structural and hydrogeological implications, *Earth and Planetary Science Letters* **204**(1-2): 249 – 263.

Rasmussen, B., Fletcher, I. R. & Sheppard, S. (2005). Isotopic dating of the migration of a low-grade metamorphic front during orogenesis, *Geology* **33**(10): 773–776.

Rial, J. A., Elkibbi, M. & Yang, M. (2005). Shear-wave splitting as a tool for the characterization of geothermal fractured reservoirs: lessons learned, *Geothermics* **34**(3): 365–385.

Rikitake, T. (1948). 1. Notes on electromagnetic induction within the Earth, *Earthquake Reasearch Institute* **24**: 1–9.

Rodi, W. & Mackie, R. L. (2001). Nonlinear conjugate gradients algorithm for 2-D magnetotelluric inversion, *Geophysics* **66**(1): 174–187.

Selway, K., Sheppard, S., Thorne, A., Johnson, S. & Groenewald, P. (2009). Identifying the lithospheric structure of a Precambrian orogen using magnetotellurics: The Capricorn Orogen, Western Australia, *Precambrian Research* **168**: 185–196.

Simpson, F. & Bahr, K. (2005). *Practical Magnetotellurics*, Cambridge University Press.

Simpson, F. & Tommasi, A. (2005). Hydrogen diffusivity and electrical anisotropy of a peridotite mantle, *Geophysical Journal International* **160**(3): 1092–1102.

Tang, C., Rial, J. A. & Lees, J. M. (2005). Shear-wave splitting: A diagnostic tool to monitor fluid pressure in geothermal fields, *Geophys. Res. Lett.* **32**(21): L21317–.

Thiel, S. (2008). *Modelling and inversion of magnetotelluric data for 2-D and 3-D lithospheric structure, with application to obducted and subducted terranes.*, PhD thesis, School of Earth and Environmental Sciences : Geology and Geophysics.

Thiel, S., Heinson, G., Gray, D. R. & Gregory, R. T. (2009). Ophiolite emplacement in NE Oman: constraints from magnetotelluric sounding, *Geophysical Journal International* **176**(3): 753–766.

Thomsen, L. (1986). Weak elastic anisotropy, *Geophysics* **51**(10): 1954–1966.

Trendall, A. F., Compston, W., Nelson, D. R., De Laeter, J. R. & Bennett, V. C. (2004). SHRIMP zircon ages constraining the depositional chronology of the Hamersley Group, Western Australia, *Australian Journal of Earth Sciences* **51**(5): 621–644.

Tyler, I. & Thorne, A. (1990). The northern margin of the Capricorn Orogen, Western Australian example of an Early Proterozoic collision zone, *Journal of Structural Geology* **12**(5–6): 685–701.

Wannamaker, P. (2005). Anisotropy Versus Heterogeneity in Continental Solid Earth Electromagnetic Studies: Fundamental Response Characteristics and Implications for Physicochemical State, *Surveys in Geophysics* **26**: 733–765.

Weckmann, U., Ritter, O. & Haak, V. (2003a). Images of the magnetotelluric apparent resistivity tensor, *Geophysical Journal International* **155**: 456–456.

Weckmann, U., Ritter, O. & Haak, V. (2003b). A magnetotelluric study of the Damara Belt in Namibia : 2. MT phases over 90 reveal the internal structure of the Waterberg Fault/Omaruru Lineament, *Physics of The Earth and Planetary Interiors* **138**: 91–112.

Weiss, C. J. & Newman, G. A. (2002). Electromagnetic induction in a fully 3-D anisotropic earth, *Geophysics* **67**(4): 1104–1114.

Wessel, P. & Smith, W. H. F. (1998). New, improved version of generic mapping tools released, *Eos Trans. AGU* **79**(47): 579–579.

Winterstein, D. F. (1990). Velocity anisotropy terminology for geophysicists, *Geophysics* **55**(8): 1070–1088.

Wülser, P. A. (2009). *Uranium metallogeny in the North Flinders Ranges region of South Australia*, PhD thesis, University of Adelaide, School of Earth and Environmental Sciences.

APPENDIX A: DETAILED METHOD

Inversion Modelling

The inversion model presented within the Two-Dimensional Modelling: Capricorn Orogen section was calculated from MT data obtained by Heinson et al. (2011) using the non-linear conjugate gradient inversion method of Rodi & Mackie (2001). MT data utilised by this inversion were collected along a line orientated 30° east from geographic north. The MT data were then rotated 60° west from geographic north such that it created an inversion model which displays the same geological structures as the forward model of the same region. In addition to this, significant masking of rotated data in both the TE-mode and TM-mode was undertaken to remove phase angles which were greater than 90° or less than 0° as they cannot be modelled using the inversion code or are considered anisotropic. This inversion used both TE and TM components of the data formed using a smoothing factor: $\tau = 3$, weighting functions: $\beta = \alpha = 1$ and error floors: $Err_{\sigma_{TE}} = 50\,\%$, $Err_{sigma_{TM}} = 20\,\%$, $Err_{\phi_{TE}} = 10\,\%$ and $Err_{\phi_{TM}} = 8\,\%$ resulting in an rms of 1.63 which could not be reduced any further by additional iterations. The modelled resistivity structure was then used to supply additional information to constrain the geological structures input into the forward model formed for the Capricorn Orogen.

Forward Modelling

All forward models presented in this study were calculated using the 2-dimensional MT direct code for conductors with arbitrary anisotropy of Pek & Verner (1997). Modelled resistivity structures were defined in terms of their principal resistivity along the x-, y- and z-axes (ρ_x, ρ_y, ρ_z respectively) defined in Ohm meters (Ωm) and their anisotropy angles strike, dip and slant (α_S, α_D, α_{SL} respectively) defined in degrees. To reduce am-

biguity and form models which approximate the true structure to the best of our knowledge, modelled resistivity structures were constrained by information interpreted from the 2-dimensional inversion models presented within the Two-Dimensional Modelling: Capricorn Orogen section and by Heinson et al. (2011) along with additional geological information (Peacock et al. 2012; Heinson et al. 2011; S. Thiel pers. comm. 2012). To further reduce ambiguity, the resistivity values assigned to each modelled structure approximated those displayed by the 2-dimensional inversion models presented within the Two-Dimensional Modelling: Capricorn Orogen section and by Heinson et al. (2011) along with known fluid resistivities (Peacock et al. 2012).

The synthetic MT responses were then plotted using Matlab codes to display phase angles in degrees and residual phase tensor ellipses. The latter containing information defining the difference between the MT response for isotropic and anisotropic resistivity structures, or pre- and post-fluid injection conditions, the orientation which experienced the greatest conductivity contrast between the two scenarios and the geometric mean of the maximum and minimum phase ($\sqrt{\triangle\phi_{max}\triangle\phi_{min}}$) which provides a measure of the phase averaged over polarisation direction (Heise et al. 2008), which are represented by the the area of an ellipse, the long axis of an ellipse and the colours used to fill the ellipses respectively.

Modelling Codes

All codes in this thesis are written in Matlab using Linux specific file paths with the exception of the 2-dimensional MT direct code for conductors with arbitrary anisotropy (2DMT) by Pek & Verner (1997) written in Fortran and the PlotPTResiduals.py code which is written in Python by Jared Peacock. Any input parameters required by the Matlab codes are input using a Graphical User Interface (GUI) pop-up window to avoid

having to set parameters manually within the code.

Input_2DMT: This code serves as a means of creating the input files for the 2-dimensional MT direct code by creating a resistivity model of the subsurface using parameters input by the user through a series of pop-up windows and a table with cells which are easily changeable. This code initially asks the user to input values which are assigned to the fields displayed in Figure 13. The spacing between adjacent mesh node in the vertical and horizontal directions for the side lobes and the surface layer are then calculated from the spacing assigned to the central block and a pop-up table of the resistivity map is displayed to the screen with dimensions in the x- and y-directions equal to the number of horizontal and vertical mesh nodes respectively. Using this table, the user then defines the thickness and width of each resistivity domain along with the anisotropic flag, principal resistivities and anisotropy angles using a series of pop-up windows. This code then outputs a .DAT file which may then be input into the 2DMT code. A list of important parameters within this code are shown below with a brief description.

- output: Defines the output .DAT file (Global variable). Coded currently as using user input however, the name may also be hardcoded within the code itself or changed later by renaming the output file. If running the 2DMT code within this code, the output .DAT file will be named the same as what is specified here and as such will require renaming also if necessary.

  The first line of input (field 1 in Figure 13) requires an integer defining the number of periods which are to be calculated for during compilation of the code. The second and third lines of input (field 2 and 3 in Figure 13) require two floats defining the lower and upper limits of the period (in seconds) which you want the

modelling code to calculate. Note, the remaining periods are defined in logarithmic space dependant on the number of periods which are to be calculated.

- period_index: Defines the number of periods which are to be calculated for during compilation of the code.

- period(i): Defines the ith period using a logarithmic scale between limiting values defined by the user.

- hor_mesh_nodes: Defines the number of horizontal mesh nodes (Global variable). Mesh steps are defined as the distances between each mesh node and as such is defined to be one value less than the number of mesh nodes.

- vert_mesh_nodes: Defines the number of vertical mesh nodes (Global variable).

- side_lobe_size: Defines the size of the side lobes and assigns the adequate number of mesh nodes.

- central_node_spacing: Defines the horizontal mesh spacing (in km) within central block (horizontal mesh step within the block).

- side_lobe_multiplier: Defines the multiplication factor for side lobes. The mesh spacing within this zone increases upon the previous mesh spacing by the multiplication factor (horizontal mesh step within the side lobes).

- vert_fine_spacing: Defines the vertical mesh spacing (in km) within the central block (vertical mesh step within the block).

- vert_fine_limit: Defines the depth limit (in km) of the central block after which the vertical multiplication factor applies.

- vert_multiplier: Defines the vertical multiplication factor for the region below the central block. The mesh spacing within this zone increases upon the previous mesh

spacing by the multiplication factor

(Mesh Spacing$_{Vertical_i}$ = Mesh Spacing$_{Vertical_{i-1}}$ × Multiplication Factor).

- surface_padding_mesh_spacing: Defines the initial vertical mesh spacing for a near surface layer.

- surface_padding: Defines the thickness (in km) of the near surface layer

- surface_padding_multiplier: Defines the multiplication factor for the vertical mesh spacing for the near surface layer. The mesh spacing within this zone increases upon the previous mesh spacing by the multiplication factor

  (Mesh Spacing$_{Surface_i}$ = Mesh Spacing$_{Surface_{i-1}}$ × Multiplication Factor).

- vert_total: Running total of the depth to an interface and is used to display depth information when defining resitivity domains using the resistivity map.

- res_map: Defines the resistivity map with dimensions in the horizontal direction equal to the number of horizontal mesh nodes and in the vertical direction equal to the number of vertical mesh nodes (Global variable). This table is then displayed using a pop-up window from which the resistivity domains are defined.

- domain_index_input: Defines the domain index associated to each resistivity domain.

- air_lobe_size: Defines the number of mesh nodes assigned to the air layer (Global variable)

- struct.: Structural variable assigned to control the following parameters (Global variable)

  - domain_total: Defines the total number of domains

– domain_index: Defines the index which the following parameters are assigned
to

* domain_index_input: Same definition as above

* Flag: Defines the anisotropic flag

* res_1: Defines the first principal resistivity

* res_2: Defines the second principal resistivity

* res_3: Defines the third principal resistivity

* res_dir_1: Defines dip anisotropy angle

* res_dir_2: Defines strike anisotropy angle

* res_dir_3: Defines slant anisotropy angle

**2-dimensional MT direct code for conductors with arbitrary anisotropy
(2DMT)**: This code, written by Pek & Verner (1997), reads the values assigned to the
fields shown in Figure 13 by the 2DMT_Input code and calculates the MT response
at the surface corresponding to each horizontal mesh node. This code then outputs a
MT_TAB_ROT.DAT file where the first four columns correspond to the site index, the
horizontal distance from the left margin of the resistivity map, period index and the
period for each station. The remaining columns correspond to the real, imaginary and
variances of the impedance tensor components and transfer functions.

loadEdi: This code, written by Stephan Thiel, reads MT data from within .edi files
and calculates the corresponding phase tensor and induction arrow components. This
code then calculates additional values and assigns the measured and calculated variables
to a set of structural variables for each station which allows for their use with the MT-
Analysis_ediDAT code.

1) Please enter the number of periods (max: 30):

2) Please enter the lower limit period in seconds:

3) Please enter the higher limit period in seconds:

4) Please enter the number of horizontal mesh nodes (max: 89):

5) Please enter the number of vertical mesh nodes (max: 89):

6) Please enter the size of side lobes (number of mesh nodes):

7) Please enter the centre block node spacing in kilometres:

8) Please enter the multiplier for side lobe node spacing:

9) Please enter the vertical node spacing within the central block in kilometres:

10) Please enter the multiplier for the vertical node spacing outside the central block:

11) Please enter the depth to the bottom of the target in kilometers:

12) Please enter the initial spacing for the surface padding in kilometers

13) Please enter the depth to the bottom of the surface padding in kilometers

14) Please enter the multiplier for the surface padding

15) Please enter the number of mesh nodes to be assigned to the air layer:

OK   Cancel

Figure 13: Image of the pop-up window created by the 2DMT_Input.m code allowing for user input.

loadDAT: This code is modified from the loadEdi code of Thiel (2008) with modifications made by Jake Macfarlane. This code initially reads the MT responses for each station from the MT_TAB_ROT.DAT file output by the 2DMT code. It then calculates the corresponding phase tensor and induction arrow components and assigns each value to a set of structural variables for each station which allows for their use with the MT-Analysis_ediDAT code.

MTAnalysis_EdiDAT: This code is modified from the MTAnalysis code of Thiel (2008) with modifications made by Jake Macfarlane. This code reads the formatted MT data output by the loadEdi and loadDAT codes along with additional formatted MT data from extra .edi and .DAT files if difference plots are to be calculated by recalling loadEdi and loadDAT, and assigns the information to a set of structural variables. The first set of files read by this code correspond to the anisotropic or post-fluid injection files whereas the second set corresponds to the isotropic or pre-fluid injection files described in this study. This code then plots the MT response for each station.

DAT2Edi: This code is modified version from the writeEdi code written by Stephan Thiel with modifications made by Jake Macfarlane. This code reads DAT files and outputs a file in an Edi format to plot phase tensor ellipses using the PlotPTResiduals.py code provided by Jared Peacock.

PlotPTResiduals.py: This code reads in synthetic or measured edi files and plots the appropriate residual phase tensor ellipses. Images produced using PlotPTResiduals.py include Figure 5, Figure 6 and 7.

MTAnalysis_Top: This code initially asks the user to specify which code the user wishes to use with the current options consisting of the MTAnalysis_EdiDAT, DAT2Edi

and Input_2DMT. Once a choice has been made, this code then reads in .edi or .DAT files and assigns them to structural variables for each station which is then passed to specified code. The files which are read by this code correspond to the post-fluid injection files described in this study.

mt2gmt: This code reads in edi files and produces a number of files in GMT format (Wessel & Smith 1998). Images produced using mt2gmt and a GMT script include Figure 2 and Figure 3.

Global Modelling Parameters

Each forward model had their MT response calculated for periods ranging from 10^{-2}s to 10^4s with five increments assigned to each decade within logarithmic space to provide equal coverage when viewing the synthetic responses in MTAnalysis_ediDAT. Each model was also defined as having an air layer fifteen mesh nodes thick above the resistivity map to avoid anomalous MT responses.

The resistivity maps for each region were defined to consist of 89 horizontal and vertical mesh nodes which were split into three sections. The first was defined to be a central block with a constant mesh spacing defined by the user situated in the middle of the model, the second was an outer region defined to be 15 mesh nodes thick on each side with mesh spacings which varied incrementally as per a multiplication factor which is defined by the user and the third was a surface layer with a thickness and mesh spacing defined by user input.

APPENDIX B: A SHORT GUIDE TO USING THE INPUT_2DMT CODE

Short Introduction

When using the 2-dimensional MT direct code for conductors with arbitrary anisotropy created by Pek & Verner (1997) it is necessary to create a resistivity map which will serve as an input file. These resistivity maps are very large and require a considerable amount of time to create successfully. To avoid this issue, I created the 2DMT_Input.m code to automate the process, significantly decreasing the time required to create the necessary files. A brief description of the 2-dimensional MT direct code for conductors with arbitrary anisotropy created by Pek & Verner (1997). Following this, a detailed outline of the 2DMT_Input.m code and the necessary input parameters will be provided.

The forward modelling code was run on Linux (Ubuntu 10.04) using the terminal whereas for Windows it was executed using NetBeans IDE 7.1.1 (available for download at http://netbeans.org/). It is also important to note that the 2DMT_Input.m code was written using Linux specific file paths and as such is currently not compatible with windows.

2DMT Forward Modelling Code

The 2-dimensional MT direct code for conductors with arbitrary anisotropy code created by Pek & Verner (1997) reads values assigned to a number of variables from an input .DAT file and calculates the surface MT response for a series of horizontal mesh node. The code then outputs a .res file and a .DAT file from which it is possible to plot synthetic MT responses.

Input Values

The input files for the 2DMT code were created using the 2DMT_Input.m code. This code requests a series of the user to input a series of values which are assigned to a set of variables which are then automatically written to a .DAT file in the format required by the 2DMT code along with an image of the modelled resistivity structure. From this, the user is then able to use manually use the 2DMT code or utilise the 2DMT hard coded within the 2DMT_Input code. To correctly run the 2DMT code within the 2DMT_Input, it is necessary to use the file names output to the Matlab command window. This was written to avoid having to alter the 2DMT source code. A list of input parameters required by the 2DMT_Input code is displayed below.

PERIOD

The first line of input (field 1 in Figure 13) requires an integer defining the number of periods which are to be calculated for during compilation of the code. The second and third lines of input (field 2 and 3 in Figure 13) require two floats defining the lower and upper limits of the period (in seconds) which you want the modelling code to calculate. Note, the remaining periods are defined in logarithmic space dependant on the number of periods which are to be calculated.

MESH NODES AND ALLOCATION

The number of mesh nodes in the horizontal, and vertical layers are defined as an integer through user input (field 4 and 5 in Figure 13) where the number of mesh nodes is equal to the number of mesh steps in the respective direction plus one. The general subsurface structure consists of three sections, a thin near-surface layer with a specific mesh spacing, thickness and mesh spacing multiplier (fields 12, 13 and 14 in Figure 13 respectively), a central block with its horizontal dimension defined by the size of the side lobes (field

6 in Figure 13) and its vertical dimension defined by the depth to the bottom of the target (11 in Figure 13) with horizontal and vertical mesh spacings defined through user input (fields 7 and 9 in Figure 13) and an outer region with horizontal and vertical mesh spacing increasing on the previous value by multiplication factors defined by the user (fields 8 and 10 in Figure 13 respectively). A series of air layers defined the region above the model which are defined to consist of a specific number of horizontal layers (field 15 in Figure 13). In this version the number of mesh nodes assigned to the air layer may be arbitrary as it is found automatically from the resistivity map however, depths are only displayed when defining the resistivity map for mesh nodes which are below the air layer defined in Figure 13.

Resistivity map

Once all the necessary fields have been filled the code will automatically generate a resistivity map with dimensions equal to the number of mesh steps in the horizontal and vertical directions where mesh steps correspond to the distance between adjacent mesh nodes. From this pop-up window it is possible to define resistivity domains within the subsurface.

Important Notes

The following section will briefly address a series of issues present within the code which affect its functionality and present means of avoiding them creating erroneous output files.

INPUT VALUES

After defining values within the pop-up window shown in Figure 13 an error message generally appears stating "Vertical mesh step too large, please redefine the vertical mesh

step multiplier." to ensure each multiplier is set a value which is able to be read by the forward modelling code. I believe an issue with this results in it appearing regardless on the orientation of the multiplier (vertical, horizontal, surface). To fix this I suggest decreasing the multiplier by 0.1 while inputting each value a number of times (I found three to work well) beginning with the original value.

RESISTIVITY MAP

It is important when defining a new resistivity domain to increase the value assigned to the resistivity domain index by one with the initial resistivity domain having to be defined using the number 1. This is because assigning a letter or previously used number to a new resistivity domain index causes errors within the code. If a complex structure is required, it is possible to generate a basic model by defining the large scale structures within the pop-up window and making additional changes to the output .DAT file.

Unincluded Variables

Further values defined within the forward modelling code which were not included in this Matlab code will be mentioned in the following sections.

BATHYMETRY INDEX

The bathymetry index is defined by two values and addresses the presence of sea water within the model. The first integer defines the number of domains defined as containing sea water with MT responses then computed on the domains lower edge (It is important to check that sea water domains are not defined as closed lenses otherwise the code can behave incorrectly). The second input then defines the domains containing sea water.

POINTS OF INTEREST

The three variables associated with the points of interest force the output MT_TAB_ROT.DAT file to output the calculated MT response at a series of specific points. The first input is an integer defining the total number of mesh nodes considered points of interests, the second input is a series of floats defining the rotation angles (in degrees) applied to the coordinates for all points of interest and the final input requires a string defining number associated with the specific mesh nodes for which you wish to calculate the surface MT response. Note, the number of rotation angles must be equal to the number of mesh nodes considered points of interest. Also, if this is not included in the input file (as is currently is), the 2DMT code outputs the unrotated MT responses for every station.

APPENDIX C: RESIDUAL PHASE TENSOR ELLIPSE

The residual phase tensors ($\mathbf{\Delta}$) presented in this study were calculated using

$$\mathbf{\Delta} = \mathbf{I} - \frac{1}{2}\left(\hat{\mathbf{\Phi}}^{-1}\mathbf{\Phi} + \mathbf{\Phi}\hat{\mathbf{\Phi}}^{-1} \right)$$

which was defined by Heise et al. (2007) where $\hat{\mathbf{\Phi}}^{-1}$ is defined as the post-fluid injection or anisotropic phase tensor and $\mathbf{\Phi}$ is defined as the pre-fluid injection or isotropic phase tensor. From this, the two of the independent invariants of the residual phase tensor are defined as

$$\Pi_1 = \frac{1}{2}\sqrt{\left(\Phi_{11} - \Phi_{22}\right)^2 + \left(\Phi_{12} + \Phi_{21}\right)^2}$$

and

$$\Pi_2 = \frac{1}{2}\sqrt{(\Phi_{11} + \Phi_{22})^2 + (\Phi_{12} - \Phi_{21})^2}$$

which then define

$$\Phi_{max} = \Pi_2 + \Pi_1$$

and

$$\Phi_{min} = \Pi_2 - \Pi_1.$$

From this it is then possible to rotate Φ_{max} and Φ_{min} to define a residual phase tensor ellipse with a major axis defined as Φ_{max} and a minor axis defined as Φ_{min} with their direction defined in the Cartesian coordinate system by

$$\alpha = \frac{1}{2}\arctan\frac{\Phi_{21} + \Phi_{12}}{\Phi_{11} - \Phi_{22}}$$

and

$$\beta = \frac{1}{2}\arctan\frac{\Phi_{12} - \Phi_{21}}{\Phi_{11} + \Phi_{22}}.$$

APPENDIX D: CAPRICORN OROGEN STATION LOCATIONS

Table 1: Location of broadband MT sites for the CP1 line from the Capricorn Orogen where masked points are defined in frequency.

Station	Long °	Long ′	Lat °	Lat ′	Elevation	Masked Points TE-mode	Masked Points TM-mode
CP1B01	117	44.557	22	28.985	639	10^2-	10^2-
CP1B02	117	41.973	22	30.269	634	All	All
CP1B03	117	39.599	22	31.305	642	10^2-	10^2-
CP1B04	117	37.738	22	33.001	653.7	10^2-	10^2-
CP1B05	117	37.092	22	35.821	603.9	10^2-	10^2-
CP1B06	117	36.898	22	38.822	584	10^2-	All
CP1B07	117	35.164	22	41.127	585	10^2-10^2	10^2-10^2
CP1B08	117	32.543	22	42.304	544	All	All
CP1B09	117	30.541	22	43.191	526.9	10^2-	10^2-
CP1B10	117	29.76	22	45.547	516.9	All	All
CP1B11	117	29.293	22	48.213	473.4	10^2-	10^2-
CP1B12	117	27.17	22	50.012	451	10^2-	10^2-
CP1B13	117	24.806	22	51.217	433	All	All
CP1B14	117	23.091	22	53.521	381	10^2-	10^2-
CP1B15	117	21.559	22	56.19	381	All	All
CP1B16	117	19.234	22	57.836	349	10^2-	10^{-2}-10^{-1},10^2-
CP1B17	117	16.944	22	58.46	343	10^2-	10^2-
CP1B18	117	13.974	22	58.632	318.4	10^2-	10^2-
CP1B19	117	11.206	22	58.193	318.4	All	All
CP1B20	117	8.569	22	58.982	318.4	All	All
CP1B21	117	5.769	22	58.073	305.6	10^2, 10^2-	10^2-
CP1B22	117	4.676	22	0.025	295.2	10^2, 10^2-	10^2-
CP1B23	117	4.204	23	2.219	285	None	None
CP1B24	117	6.148	23	4.177	290	10^2-	10^2, 10^2-
CP1B25	117	8.246	23	6	285	All	All
CP1B26	117	8.475	23	9.233	279	10^2-	10^2-
CP1B27	117	7.831	23	11.656	260	10^2-	10^2-
CP1B28	117	8.421	23	14.329	256	10^2, 10^2-	10^2-
CP1B29	117	8.023	23	16.131	240	All	10^2-
CP1B30	117	5.168	23	17.56	238	10^2, 10^2-	10^2-
CP1B31	117	3.189	23	19.408	235	All	10^2-
CP1B32	117	2.179	23	21.7	237	None	None
CP1B33	117	3.161	23	23.853	242	10^2-	10^2-
CP1B34	117	5.778	23	25.152	240	10^2-	10^2-
CP1B35	117	7.668	23	26.823	250	10^2-	10^2-
CP1B36	117	9.175	23	29.01	248	10^2-	10^2-
CP1B37	117	8.359	23	30.997	258	10^2-	10^2-
CP1B38	117	11.644	23	33.251	263	10^2-	10^2-
CP1B39	117	11.246	23	35.846	276	All	10^2-